



**HAL**  
open science

# Ice Concentration Retrieval from the Analysis of Microwaves: Evaluation of a New Methodology Optimized for the Copernicus Imaging Microwave Radiometer

Catherine Prigent, Lise Kilic, Filipe Aires, Victor Pellet, Carlos Jimenez

► **To cite this version:**

Catherine Prigent, Lise Kilic, Filipe Aires, Victor Pellet, Carlos Jimenez. Ice Concentration Retrieval from the Analysis of Microwaves: Evaluation of a New Methodology Optimized for the Copernicus Imaging Microwave Radiometer. *Remote Sensing*, 2020, 12 (10), pp.1594. 10.3390/rs12101594. hal-03045716

**HAL Id: hal-03045716**

**<https://hal.sorbonne-universite.fr/hal-03045716>**

Submitted on 13 Dec 2020

**HAL** is a multi-disciplinary open access archive for the deposit and dissemination of scientific research documents, whether they are published or not. The documents may come from teaching and research institutions in France or abroad, or from public or private research centers.

L'archive ouverte pluridisciplinaire **HAL**, est destinée au dépôt et à la diffusion de documents scientifiques de niveau recherche, publiés ou non, émanant des établissements d'enseignement et de recherche français ou étrangers, des laboratoires publics ou privés.

Article

# Ice Concentration Retrieval from the Analysis of Microwaves: Evaluation of a new methodology optimized for the Copernicus Imaging Microwave Radiometer

Catherine Prigent <sup>1,2</sup>, Lise Kilic <sup>1</sup>, Filipe Aires <sup>1,2</sup>, Victor Pellet <sup>1,2</sup>, and Carlos Jimenez <sup>2,1</sup>

<sup>1</sup> Sorbonne Université, Observatoire de Paris, Université PSL, CNRS, LERMA, Paris, France

<sup>2</sup> Estellus, Paris, France

\* Correspondence: catherine.prigent@obspm.fr

Version May 7, 2020 submitted to Remote Sens.

**Abstract:** A new methodology has been described in Kilic *et al.* [1] (Part 1 of this study) to estimate Sea Ice Concentration (SIC) from satellite passive microwave observations between 6 and 36 GHz. The Ice Concentration REtrieval from the Analysis of Microwaves (IceCREAM) algorithm is based on optimal estimation, with a simple radiative transfer model derived from satellite observations at 0 and 100% SIC. Observations at low and high frequencies have different spatial resolutions, and a scheme is developed to benefit from the low errors of the low frequencies and the high spatial resolutions of the high frequencies. This effort is specifically designed for the Copernicus Imaging Microwave Radiometer (CIMR) project, equipped with a large deployable antenna to provide a spatial resolution of ~5 km at 18 and 36 GHz, and ~15 km at 6 and 10 GHz. The algorithm is tested with AMSR2 observations, for a clear scene over the north polar region, with collocated MODIS estimates and the OSI SAF operational product. Several algorithm options are tested, and the study case shows that both high spatial resolution and low errors are obtained with the IceCREAM method. It is also tested for the full polar regions, winter and summer, under clear and cloudy conditions. Our method is globally applicable, without fine-tuning or further weather filtering. The systematic use of all channels from 6 to 36 GHz makes it robust to changes in ice surface conditions and to weather interactions.

**Keywords:** Sea ice concentration; Passive microwaves; Inversion; Optimal estimation; Copernicus Imaging Microwave Radiometer

## 1. Introduction

Since 1979, Arctic sea ice extent has decreased all year long, with a September sea ice reduction of ~12% per decade (e.g., [2,3]). In the Arctic, surface air temperature increased by more than double the global average over the last two decades (the so-called Arctic amplification issue [4,5]). Changes in Arctic sea ice have the potential to influence weather and climate not only at regional scales but also at large scales (e.g., [6–8]).

The Sea Ice Concentration (SIC) has been retrieved from satellite microwave radiometer data for ~40 years, and the daily estimates of the global sea ice extent from these observations are one of the longest continuous climate records (e.g., [9]). Current microwave SIC algorithms rely on empirical methods, using the difference in radiometric signatures between the open ocean and the sea ice, based on the fact that the ocean emissivity is significantly lower than the sea ice emissivity, between 6 and 90 GHz. The retrieval algorithms are derived from coincident data sets of satellite observations and in situ measurements (such as the Round Robin Data Package (RRDP) [10]) with fully ice covered sites

32 (100% SIC) and purely open ocean areas (0% SIC), called tie points. Historical algorithms include the  
33 NASA/TEAM algorithm [11], the Bootstrap algorithm [12] or the Bristol algorithm [13]. More recent  
34 algorithms use combinations of these methods [9,14], with a limited number of channels to estimate  
35 the SIC. Most of them are based on channels at 18 and 36 GHz. An evaluation of an ensemble of SIC  
36 algorithms showed that the algorithm using 6.9 GHz observations had the lowest error [15], because  
37 that frequency is less affected by the atmosphere and by the snow cover than the higher frequencies.

38 A new methodology has been described in detail in Kilic *et al.* [1] to estimate the  
39 SIC from satellite passive microwave observations between 6 and 36 GHz, on board conical  
40 imagers (in the following that companion paper will be called Part 1). The Ice Concentration  
41 REtrieval from the Analysis of Microwaves (IceCREAM) algorithm is based on an optimal  
42 estimation method, based on a simple radiative transfer model derived from the RRDP.  
43 Observations at low and high frequencies having different spatial resolutions, a scheme is  
44 designed to benefit from the low errors of the low frequencies and the high spatial resolutions  
45 of the high frequencies. This effort is specifically designed for the Copernicus Imaging  
46 Microwave Radiometer (CIMR) project [16]. For an extensive description of the mission,  
47 see <https://cimr.eu/sites/cimr.met.no/files/documents/CIMR-MRD-v2.0-20190305-ISSUED0.pdf>.  
48 This mission is one of six High Priority Candidate Missions within the Copernicus Expansion  
49 programme, identified by the European Commission as priorities in the coming years to provide  
50 additional capabilities in support of user needs. CIMR will be equipped with a foldable antenna of  
51  $\sim 7$  m diameter and low-noise receivers at 1.4, 6.9, 10.65, 18.7, and 36.5 GHz, in vertical and horizontal  
52 polarizations. It will observe with an incidence angle of  $55^\circ$  from an orbit at  $\sim 830$  km, with a  $\sim 1900$  km  
53 swath and a full coverage of the Poles. It will provide a spatial resolution of  $\sim 5$  km at 18 and 36 GHz,  
54  $\sim 15$  km at 6 and 10 GHz, and  $\sim 55$  km at 1.4 GHz.

55 Here, the new SIC retrieval [1] is tested with observations from the Advanced Microwave  
56 Scanning Radiometer 2 (AMSR2), on board the Japanese JAXA GCOM-W1 mission. AMSR2 provides  
57 observations at frequencies between 6 and 36 GHz, in both vertical and horizontal polarizations, with  
58 an incidence angle of  $55^\circ$ , but with coarser spatial resolution than the CIMR instrument. AMSR2  
59 has 7.3, 23.8, and 89.0 GHz channels in addition to the CIMR ones, but it does not have the 1.4 GHz  
60 channels. The 1.4 GHz is not used here for SIC estimate, essentially because of its low spatial resolution  
61 ( $\sim 55$  km). The characteristics of the channels that are common to CIMR and AMSR2 and used in this  
62 study for the evaluation of the SIC are indicated in Table 1. The instrument noise (the radiometric  
63 resolution also called the Noise equivalent  $\Delta T$ ,  $Ne\Delta T$ ) is not a key issue as the sensitivity of the  
64 observation to the SIC signal is large compared to the instrument noise.

65 Variations of the new method are tested here, to illustrate the impact of the different algorithm  
66 parameters: the frequency selection, changes in the statistical dataset to derived the 0 and 100% SIC  
67 (the so-called tie points), the effect of the fusion of the low and high frequencies to reduce the error  
68 and improve the spatial resolution. Our goal at this stage is not to develop an operational algorithm,  
69 but to assess the methodology, toward the optimization of an algorithm for the CIMR mission.

70 First, the methodology is applied to AMSR2 observations for one clear sky scene over the north  
71 polar region and compared to SIC estimates from visible / near-infrared Moderate Resolution Imaging  
72 Spectroradiometer (MODIS) imagery. The operational SIC product from the EUMETSAT Ocean Sea  
73 Ice - Satellite Application Facilities (OSI SAF, [www.osi-saf.org](http://www.osi-saf.org)), derived from AMSR2 observations, is  
74 also examined [9,14]. Second, evaluations are performed at large scales, over north and south polar  
75 regions, during both winter and summer.

76 Section 2 summarizes the methodology and presents the satellite observations and products. In  
77 Section 3, the results are assessed locally over a boreal region under clear sky conditions, whereas large  
78 scale results are discussed in Section 4. Section 5 concludes this study, insisting on the future potential  
79 developments.

**Table 1.** The CIMR instrument specifications with a 7 m diameter antenna, as compared to the characteristics of the AMSR2 current instruments, for their common frequencies used in this study. The central frequency, the spatial resolution, the incidence angle, as well as the instrument noise ( $Ne\Delta T$ ) are indicated.

Instrument	Frequency (GHz)	Spatial resolution (km)	Incidence angle ( $^{\circ}$ )	$Ne\Delta T$ (K)
CIMR	6.9	15	55	0.2
CIMR	10.65	15	55	0.3
CIMR	18.7	5	55	0.3
CIMR	36.5	5	55	0.7
AMSR2	6.9	48	55	0.3
AMSR2	10.65	33	55	0.6
AMSR2	18.7	18	55	0.6
AMSR2	36.5	9	55	0.6

## 80 2. Method and Materials

### 81 2.1. The IceCREAM algorithm

82 This new methodology is particularly adapted for the CIMR mission. It follows the optimal  
 83 estimation scheme that is often adopted for the retrieval of geophysical parameters from satellites  
 84 [17]. It is very flexible and allows using different channel combinations to retrieve the SIC. The  
 85 method requires a forward model that establishes the relationship between the SIC and the brightness  
 86 temperatures (TBs) measured by the satellite. The forward model is empirically based on the contrast  
 87 between ocean and ice TBs. The mean TBs for the open ocean (corresponding to 0% SIC) and for the  
 88 total ice cover (corresponding to 100% SIC) are estimated from the collection of passive microwave  
 89 observations contained in the RRDP. Then, the forward model is simply a linear mixing model derived  
 90 from the TB contribution of the two extreme surface types within the sensor footprint. With the optimal  
 91 estimation scheme, a theoretical retrieval error is systematically attached to each inversion.

92 Tests have been performed using different combinations of channels between 6 and 36 GHz. The  
 93 algorithm with the 6 and 10 GHz (both vertical and horizontal polarizations) is rather insensitive  
 94 to changes in the sea ice environments, with a low theoretical retrieval error. However, these low  
 95 frequency channels only provide low spatial resolution estimates. The algorithm using the 18 and  
 96 36 GHz (both vertical and horizontal polarizations) shows larger retrieval errors, but with an improved  
 97 spatial resolution.

98 The CIMR mission will provide the same spatial resolution (15 km) for the 6 and 10 GHz channels,  
 99 and the same spatial resolution (5 km) for the 18 and 36 GHz channels. The IceCREAM algorithm  
 100 proposes a method to combine the SIC estimate at high resolution using the 18 and 36 GHz channels,  
 101 with the low resolution estimation using the 6 and 10 GHz channels. The SIC estimate at low resolution  
 102 is used to correct the SIC estimates at high resolution that are within the low resolution pixel, using a  
 103 data fusion scheme.

104 More detail about the IceCREAM method is provided in Kilic *et al.* [1] (Part 1 of this study).

### 105 2.2. MODIS sea ice

106 MODIS instrument observes the Earth from visible to infrared wavelengths. With its polar orbit  
 107 and large swath ( $\sim 2300$  km), it frequently covers the polar regions. Under clear sky conditions,  
 108 presence of sea ice can be detected from MODIS, using combination of thresholds on the observed  
 109 reflectances in the visible and near-infrared bands. For comparison with the passive microwave SIC  
 110 products, the sea ice day product from MODIS on board the Aqua mission (MYD29P1D) at 1 km spatial  
 111 resolution is selected here, as provided by the National Snow and Ice Data Center (NSIDC) [18]. Each  
 112 oceanic 1 km pixel is classified as ice, ocean, or cloud. A predominantly clear sky case over the north



113 polar region is selected, on April 4, 2018, and the corresponding NSIDC MODIS sea ice product is  
 114 downloaded. Figure 1 (left) presents the NSIDC MODIS sea ice product for the selected situation over  
 115 the north polar region. The sea ice cover is showing large discontinuities in the Davis Strait, between  
 116 the Baffin Island and Greenland. Although not visible at the resolution of the figure, the ice edges are  
 117 often contaminated by clouds in the MODIS products. This is partly explained by cold winds blowing  
 118 from sea ice to ocean and generating clouds at the contact with the 'warm' ocean. It could also be  
 119 partly related to algorithm problems in these transition zones. Other situations have been analyzed  
 120 but are not shown here.

121 The MODIS sea ice product is spatially averaged over the AMSR2 footprints, to produce a  
 122 MODIS-derived SIC estimate comparable with the AMSR2 SIC products. Figure 1 (right) presents the  
 123 results at the 18 GHz spatial resolution for the selected image (18 km at this frequency, see Table 1). The  
 124 MODIS SIC within an AMSR2 footprint is calculated as the ratio between the number of MODIS sea  
 125 ice pixels versus the sum of sea ice pixels and ocean pixels, without counting the cloudy 1 km pixels.  
 126 Different thresholds on the number of acceptable cloudy pixels within the AMSR2 footprint have  
 127 been tested. If no cloudy pixels are tolerated, MODIS-derived SIC at AMSR2 resolution can seldom  
 128 be calculated around the ice edges. On the contrary, if a very large fraction of clouds is accepted,  
 129 the MODIS-derived SIC is meaningless. Several tests showed that a threshold of 50% on the cloud  
 130 percentage in the AMSR2 footprint was providing acceptable results, even over the ice edges.

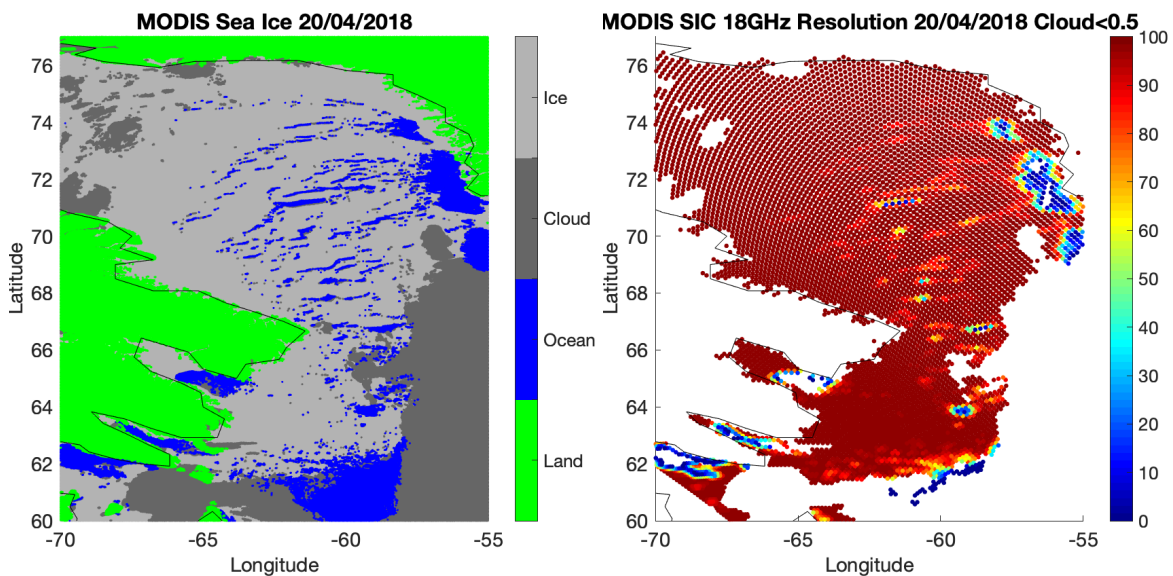


**Figure 1.** The MODIS sea ice information for the selected scene, 20/04/2018. Left: the original MODIS sea ice data at 1 km spatial resolution. Right: the MODIS-derived Sea Ice Concentration (SIC), as calculated from spatial averaging over the 18 GHz AMSR2 footprint, when the cloud cover is less than 50%. The landmasses are Greenland in the north-east of the image and Baffin Island in the west.

### 131 2.3. AMSR2

132 The AMSR2 instrument has already been briefly described (Table 1). The AMSR2 data are  
 133 extracted from the JAXA data center ([https://suzaku.eorc.jaxa.jp/GCOM\\_W/index.html](https://suzaku.eorc.jaxa.jp/GCOM_W/index.html)). The level  
 134 L1R product is used [19]. To mimic the fact that the CIMR instrument has the same spatial resolution at  
 135 6 and 10 GHz and at 18 and 36 GHz respectively, the 10 GHz observations are spatially averaged to the  
 136 6 GHz resolution, and the 36 GHz observations are averaged to the 18 GHz footprint, all provided by  
 137 the L1R dataset. The observations are sampled at 12 km. Figure 2 shows the 6 and 36 GHz brightness  
 138 temperature (TB) images at vertical polarization, for the selected situation. The 6 GHz observations  
 139 are displayed at their nominal resolution and the 36 GHz observations at the 18 GHz resolution. As

140 discussed in Part 1, among the selected frequencies, the 6 and 36 GHz frequencies have respectively  
 141 the highest and the lowest sensitivity to the presence of ice. The spatial structures in Figure 2 are very  
 142 similar to the sea ice extent derived from the MODIS images (see Figure 1), emphasizing the sensitivity  
 143 of these observations to the presence of sea ice. Even directly on the TB maps, the discontinuities in the  
 144 sea ice cover are observable. The different sensitivities to the sea ice at 6 and 36 GHz are obvious, with  
 145 much more contrast between the ocean and sea ice TBs at 6 than at 36 GHz. More small structures are  
 146 observed with the 36 GHz, especially at the sea ice edge, as expected from the better spatial resolution  
 147 at this frequency. Note that at 6 GHz vertical polarization, continental ice has very similar signatures  
 148 than the sea ice, at least close to the coasts in this region.

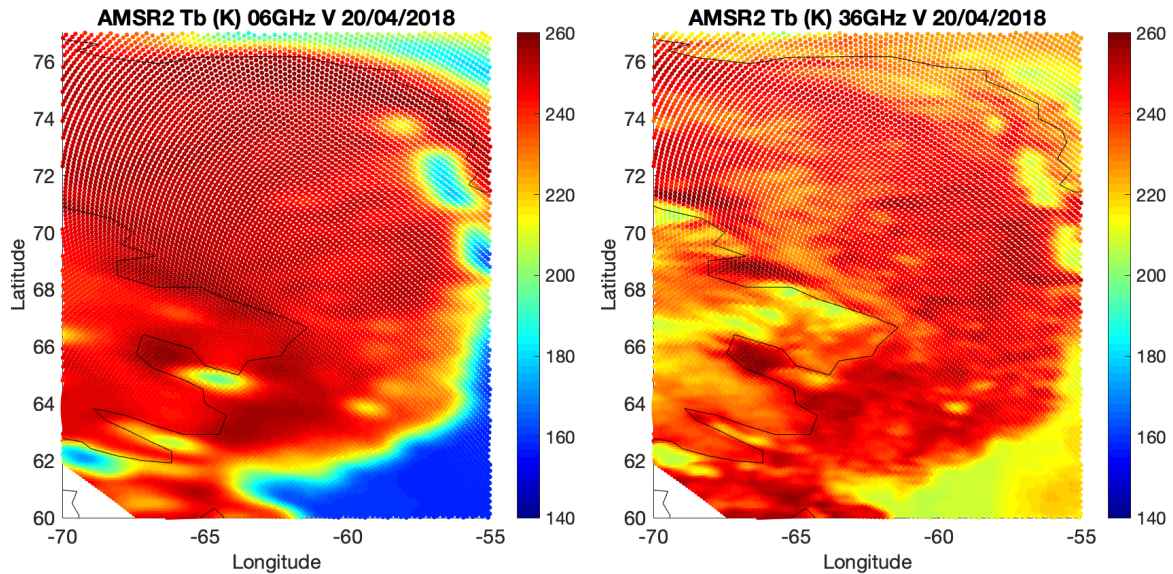


**Figure 2.** The AMSR2 data for the selected scene, 20/04/2018. Left: the 6 GHz vertical polarization (at its nominal spatial resolution). Right: the 36 GHz vertical polarization (at the 18 GHz spatial resolution).

#### 149 2.4. OSI SAF SIC

150 The AMSR2 sea ice concentration product of the OSI SAF (OSI-408) is compared to the IceCREAM  
 151 estimates. The OSI SAF Hybrid Dynamic product is extracted for the selected situation, as well as for  
 152 large scale comparisons for both north and south polar regions. The algorithm uses 18 and 36 GHz  
 153 observations at vertical polarization. It is a combination of the NASA Bootstrap algorithm [12,20]  
 154 for low SIC and the Bristol algorithm [13] for high SIC. It includes water vapor correction over the  
 155 ocean, using Numerical Weather Prediction analysis and a radiative transfer model. To account for  
 156 their time variations, the algorithm anchor points (also called the tie points) for pure sea ice and open  
 157 ocean are regularly updated. Filters and masks are further applied to avoid algorithm artifacts (along  
 158 coast lines for instance). The product is available on a 10km polar stereographic grid. An uncertainty  
 159 assessment is attached to each SIC estimate: it includes the intrinsic algorithm uncertainty and the  
 160 so-called smearing uncertainty due to the sampling of different frequency footprints onto a single grid.  
 161 For a full description of the dynamic hybrid algorithm and the derived dataset, see [9,14].

162 For the selected scene, the OSI SAF SIC is presented in Figure 3, along with its total uncertainty  
 163 (the sum of the algorithm and smearing uncertainties). The spatial structures of the OSI SAF SIC are in  
 164 very good agreement with the SIC estimates from MODIS (Figure 1). Note that the total uncertainty is  
 165 dominated by the smearing uncertainty, with a maximum of  $\sim 5\%$  in the algorithm uncertainty (not  
 166 shown).

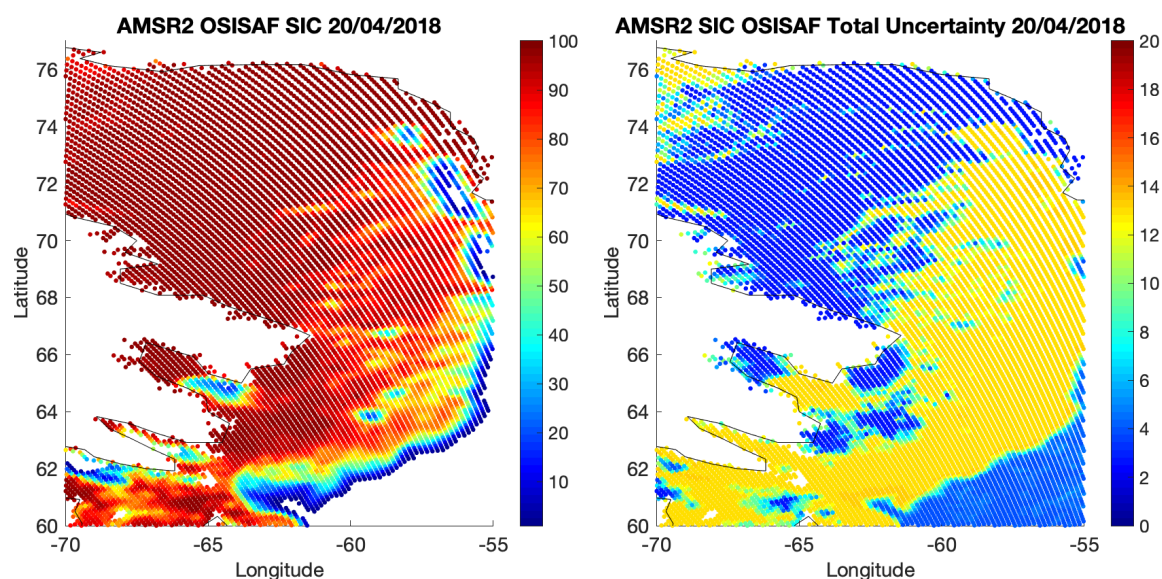


**Figure 3.** The OSI SAF results for the selected scene, 20/04/2018. Left: the sea ice concentration (SIC). Right: the total uncertainty on that product (the sum of the algorithm and smearing uncertainties).

### 167 3. Results and discussion for a local scene

168 For the selected situation, the SIC estimates are tested with different algorithm choices. First, the  
 169 frequency selection is assessed. Second, the impact of the tie points is evaluated, and finally, the fusion  
 170 of the low and high resolution results is examined. Note that other local scenes have been studied,  
 171 with similar results.

#### 172 3.1. Frequency selection and sensitivity to the tie points

173 First, the inversion algorithm is applied to the combination of the 6 and 10 GHz channels and  
 174 the 18 and 36 GHz channels, respectively, using both perpendicular polarizations for all considered  
 175 frequencies (named 6+10GHz and 18+36GHz algorithms in the following). The Round Robin Data  
 176 Package (RRDP) [10] is a database of satellite observations at 0 and 100% SIC (see Part 1 for more  
 177 information on its use here). The full RRDP is used to derive the sensitivity of the observations to  
 178 the SIC (north and south polar regions, for all seasons). The algorithm theoretical error standard  
 179 deviations (StDs) are also systematically calculated, as described in Part 1. As already mentioned,  
 180 the observations are considered at the spatial resolution of the lower frequency channel used in the  
 181 algorithm (i.e., for the 18+36GHz combination, the 36 GHz observations are averaged on the 18 GHz  
 182 spatial resolution and for the 6+10GHz combination, the 10 GHz observations are averaged on the  
 183 6 GHz spatial resolution). Note that in current SIC operational algorithms (OSI SAF for instance), each  
 184 observation is used at its original resolution and the spatial resolution issue is accounted for by an  
 185 additional term in the error budget (the smearing error) [14].

186 Figure 4 presents the results of the retrievals, along with the algorithm theoretical error StDs.  
 187 The results of our 18+36GHz algorithm appear very similar to the OSI SAF results (Figure 3) (despite  
 188 their different projections: our results are provided at the swath level whereas the OSI SAF results are  
 189 gridded on a 10 km polar stereographic grid). It is also clear that the 18+36GHz algorithm provides  
 190 better spatial resolution than the 6+10GHz combination, with very blurred structures for the 6+10GHz  
 191 combination. However, the associated theoretical error Std is significantly better for the 6+10GHz  
 192 algorithm than for the high frequency one, as expected.

193 To better quantify the differences between the retrievals, the histograms of the SIC distributions  
 194 are provided in Figure 5, for the MODIS estimates at the spatial resolution of the AMSR2 18 GHz, for



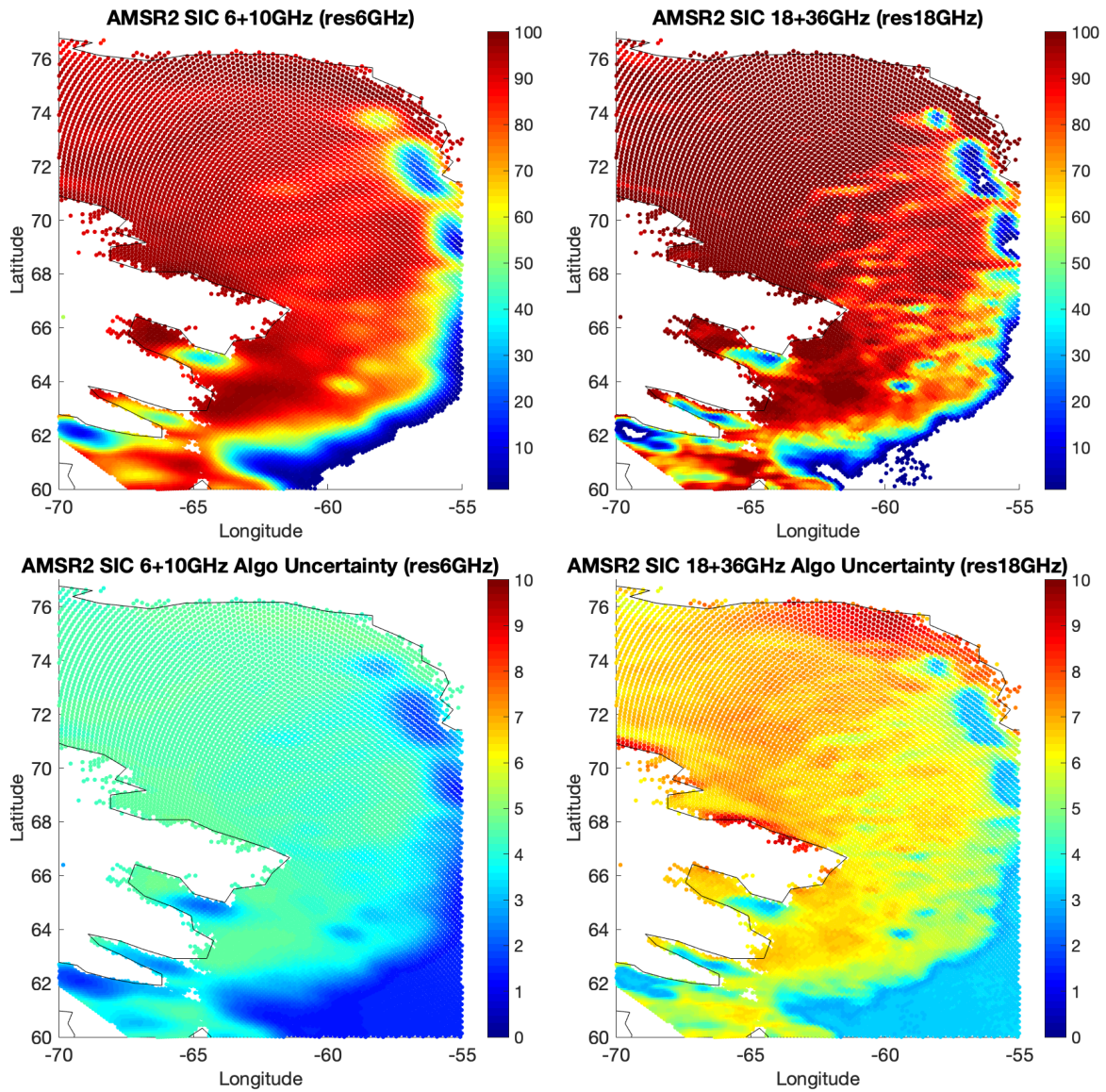


**Figure 4.** SIC retrieval results for the 20/04/2018 scene, along with the corresponding algorithm theoretical error StD. Top: for the 6+10GHz combination (the SIC on the left and the corresponding error on the right). Bottom: same for the 18+36GHz combination.

195 the 6+10GHz and 18+36GHz retrievals we developed using the full RRDP (solid lines). The pixels that  
196 are cloud contaminated at more than 50% are excluded for the comparisons, as estimated by MODIS.  
197 The MODIS estimates show very large populations at 0 and 100%, and a limited population with  
198 partial ice cover. This is partly related to the fact that the sea ice edges are often cloudy, but also likely  
199 to some ambiguities in the detection of sea ice edges and clouds with MODIS as already mentioned.  
200 AMSR2 estimates have broader peaks, especially around 100% for the 18+36GHz algorithms. The  
201 maxima of these peaks are not at 0 or 100%, with some pixels below 0% and a significant population of  
202 pixels above 100% for the 18+36GHz algorithm. This is in agreement with the results from Part 1 that  
203 showed that the 18+36GHz algorithms have larger systematic and random errors than the 6+10GHz  
204 combinations. Note nevertheless that the peaks of the 6+10GHz distribution are not strictly at 100%  
205 and 0% as expected, but rather are shifted slightly below 100% and slightly above 0%: the 6+10GHz  
206 algorithm is expected to provide unbiased results at a global scale, averaged over a full seasonal cycle,  
207 as described by the full RRDP (see Part 1). Here, only one scene is presented, for the north polar region  
208 at a given time in the year, and some bias is observed as the responses of the 6 and 10 GHz to the  
209 sea and ice conditions in this specific situation do not perfectly match the averaged conditions in the  
210 RRDP.

211 Changes in the tie points (dynamic tie points) have been applied in operational method such as the  
212 OSI SAF algorithm, to account for the impact of the sea ice variability on the microwave observations  
213 as a function of location and season. Here, the effect of modifying the tie points is tested in our  
214 algorithm by selecting only part of the full RRDP to derive the sensitivity of the observations to the  
215 SIC. Only the situations collected over the north polar region are selected, first for the winter months,  
216 then for the summer months. The histograms of the SIC results for the same scene are presented in  
217 Figure 5 (dashed lines), as compared to the results using the full RRDP (solid lines). Some changes  
218 are observed in the SIC distributions, both for the 6+10GHz and 18+36GHz algorithms, but they are  
219 limited, confirming the results obtained in Part 1. From now on, the sensitivity of the observations will  
220 be derived from the full RRDP (both polar regions, all seasons).

221 Under this clear sky situation, the 6+10GHz algorithm already shows lower errors than the  
222 18+36GHz combination. It is expected that the low frequency algorithm would even be more beneficial  
223 for cloudy scenes, as clouds mostly affect the high frequencies.

### 224 3.2. Fusion of the retrievals at low and high resolutions

225 There is a ratio of 3 in the spatial resolutions of the 6 and 18 GHz for both AMSR2 and CIMR  
226 instruments. The CIMR instrument is designed to have the same ~15 km spatial resolution at 6 and  
227 10 GHz, and the same ~5 km spatial resolution at 18 and 36 GHz, to facilitate the combination of the  
228 low and high frequency channels, respectively. Here, we test the methodology described in Part 1 to  
229 combine the large sensitivity of the 6+10GHz algorithm to the SIC with the high spatial resolution of  
230 the 18+36GHz retrieval.

231 The IceCREAM methodology consists in performing the retrieval separately for the lower  
232 frequencies (6+10GHz) and the higher frequencies (18+36GHz) first, and then in using the low  
233 frequency retrieval to de-bias all the high frequency retrievals that fall within the low frequency / low  
234 spatial resolution retrieval. The lower frequency retrieval provides good accuracy and precision but  
235 with low spatial resolution. On the contrary, the high frequency retrieval has good spatial resolution,  
236 but with large errors. The solution consists in averaging each individual high spatial resolution  
237 retrieval within a low resolution pixel, to fit the low resolution retrieval. The averaging takes into  
238 account the respective uncertainty of the individual high spatial resolution retrieval. This can be seen  
239 as a disaggregation of the low frequency retrieval, using the high frequency retrieval at high spatial  
240 resolution. This solution is particularly well suited for CIMR, as the low frequency channels at 6  
241 and 10 GHz (respectively high frequency channels at 18 and 36 GHz) will have very similar spatial  
242 resolutions, i.e., their combination (6 and 10 GHz on one side and 18 and 36 GHz on the other side)  
243 will not raise any spatial resolution issue, providing a final product at the high spatial resolution. For

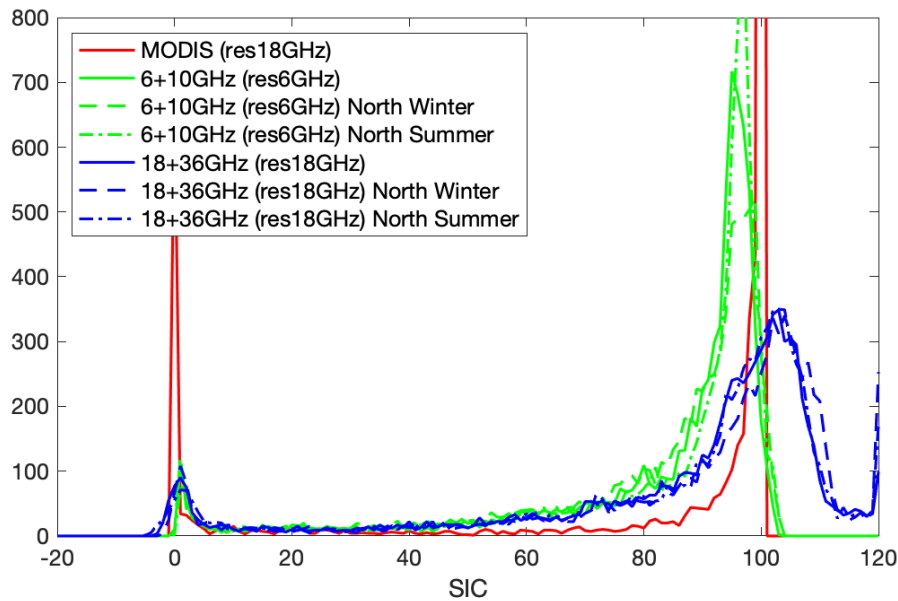


**Figure 5.** For the 20/04/2018 scene, the histograms of the SIC for MODIS at 18 GHz resolution in red, for our algorithms using the full RRDP with 6+10GHz in green (solid line), and for 18+36GHz in blue (solid line). Comparisons of our 6+10GHz and 18+36 GHz AMSR2 algorithms using different subsets of the RRDP are also presented: limited to the north polar region for the winter season (dash lines) and then limited to the north polar region for the summer season (dash-dotted lines). The pixels that are cloud contaminated at more than 50% are excluded, as estimated by MODIS.

244 the same local scene, the previous results of the 18+36GHz retrieval are tuned to match the coinciding  
 245 results at 6+10GHz, taking into account the respective errors of the results, following the method  
 246 developed in Part 1. The map of the SIC results is presented in Figure 6, along with the corresponding  
 247 error StD. For the same scene, Figure 6 also shows the difference between the MODIS SIC (as calculated  
 248 from spatial averaging over the 18 GHz AMSR2 footprint, when the cloud cover is less than 50%) and  
 249 the IceCREAM SIC results. Over regions of high (close to 100%) and low (close to 0%) SIC, limited  
 250 differences are observed between MODIS and IceCREAM SIC. However, in regions of intermediate  
 251 SIC (see for instance the large differences around 62°N or around -57°E), the differences are significant.  
 252 This can be related to the use of the linear forward model in the retrieval that implicitly assumes that  
 253 the microwave response to the sea ice is the same regardless of the ice nature between 0% and 100%  
 254 SIC. Around the ice margin, the ice physical characteristics are likely different, with impact on the ice  
 255 microwave responses, leading to errors in the microwave SIC. In addition, as already mentioned, the  
 256 MODIS SIC estimates also show limitations in the ice margin areas, with ambiguities with cloud cover.

257 For a more detailed assessment of the results, the histograms of the resulting SIC distribution  
 258 is shown, compared to the MODIS estimates at 18 GHz resolution and the 6+10GHz and 18+36GHz  
 259 algorithms (Figure 7). The distribution of the results for the fusion of the 6+10GHz and 18+36GHz  
 260 algorithms (the all channel results) is close to the results at 6+10GHz, with low bias and a limited  
 261 dispersion around the maximum, especially close to 100% SIC. In addition, Figure 8 presents a  
 262 comparison of the SIC estimates over two transects for the scene, at 62°W and 59°W. The following  
 263 products are evaluated: the MODIS estimates at 18 GHz resolution, our AMSR2 6+10GHz and  
 264 18+36GHz retrievals, our retrieval combining all the frequencies (fusion of the 6+10GHz and 18+36GHz  
 265 retrievals), and the OSI SAF operational products.

266 All the AMSR2-derived SIC retrievals follow reasonably well the MODIS estimates. Our SIC  
 267 estimates with the 18+36GHz algorithm are in good agreement with the OSI SAF operational product  
 268 (also derived from the same frequencies), although we do not apply any tie point changes nor any



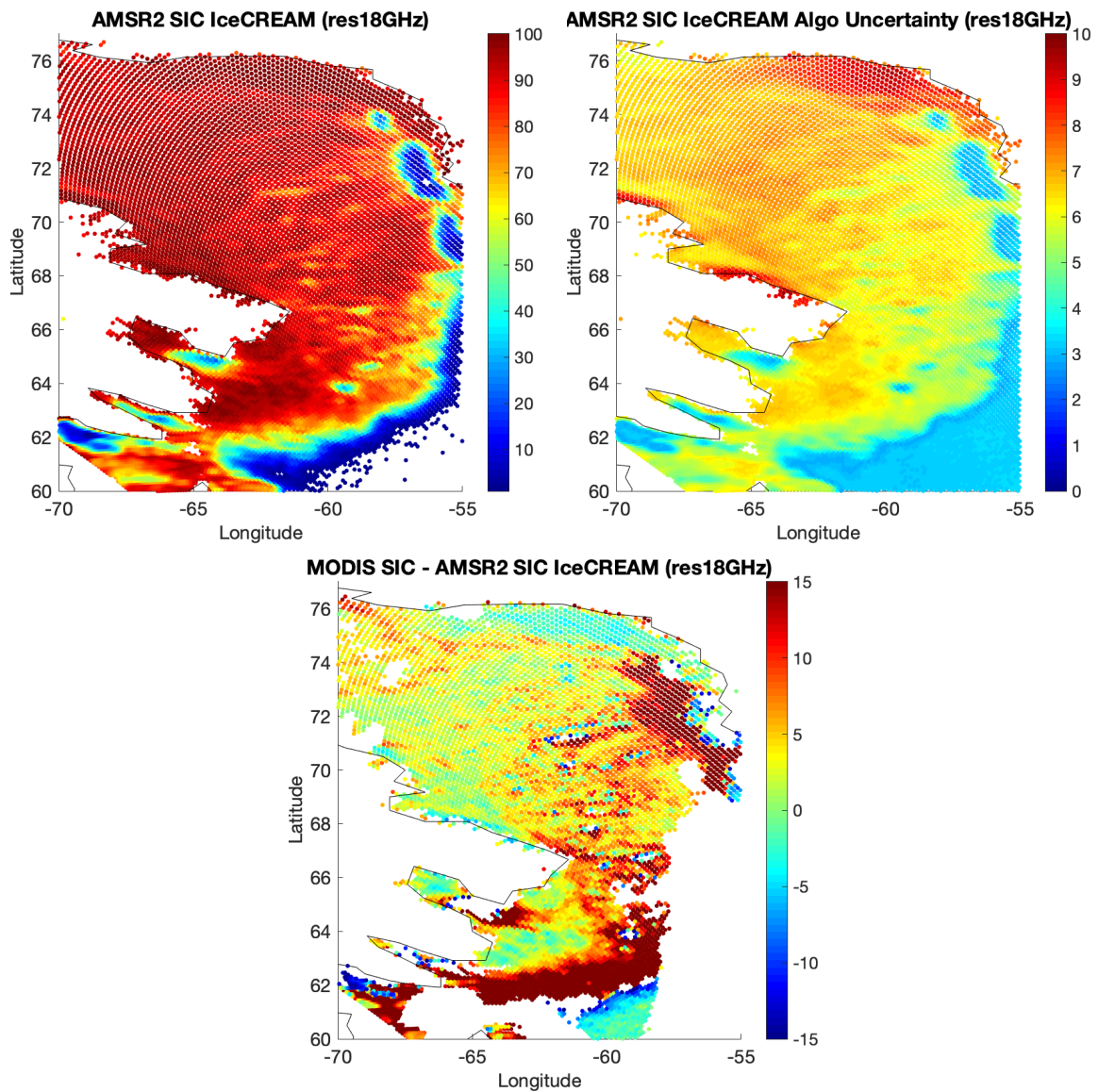


**Figure 6.** Top left: IceCREAM SIC retrieval results for the 20/04/2018 scene, when combining all the channels, i.e., the low (6+10GHz) and the high (18+36GHz) frequency algorithms. Top right: the corresponding theoretical retrieval error StD. Bottom: Difference between the MODIS SIC and the IceCREAM SIC results. The MODIS SIC is calculated from spatial averaging over the 18 GHz AMSR2 footprint, when the cloud cover is less than 50% (leading to holes in the image).

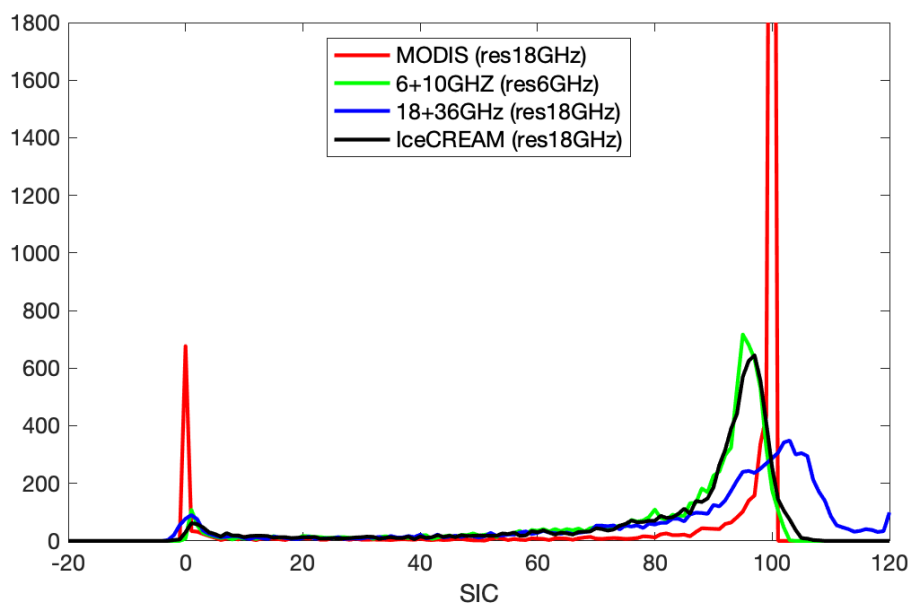


**Figure 7.** For the 20/04/2018 scene, the histograms of the SIC for MODIS at 18 GHz resolution in red, for our 6+10GHz AMSR2 algorithm in green, for our 18+36GHz AMSR2 algorithm in blue, and for the IceCREAM retrieval (all channel algorithm in black). The pixels that are cloud contaminated at more than 50% are excluded, as estimated by MODIS.

269 weather filtering on our results. We deliberately do not adopt a threshold at 0% and 100% on our SIC,  
 270 to illustrate the uncertainties related to our 18+36GHz algorithm: in operational mode, thresholds  
 271 would obviously be applied. With the 6+10GHz algorithm, the spatial structures are clearly smeared,  
 272 as compared to the other products with higher spatial resolution. Combining all the frequencies  
 273 provides results that show the spatial resolution of the 18+36GHz combination, but with values closer  
 274 to the 6+10GHz algorithm that has been shown to have less systematic and random errors.

#### 275 4. Results and discussion at large scales over the polar regions

276 The method is tested at large scales over the north and south polar regions, for both winter and  
 277 summer. The previous case study was limited to clear sky conditions, for comparison with MODIS  
 278 data. It focussed on the Arctic at the end of the winter. Here, both clear and cloudy situations are  
 279 considered, for two seasons, and for both polar regions. The same collection of observations from  
 280 the full RRDP is used to estimate the sensitivity of the microwave observations to the SIC, for both  
 281 hemispheres and seasons.

282 Two days are selected, January 30, 2018 and August 30, 2018. The following estimates are  
 283 compared: our 6+10GHz and 18+36GHz algorithms, the combination of these two results (the all  
 284 channel IceCREAM results), and the original OSI SAF estimates. Figures 9 and 10 present the results  
 285 for the north and south polar regions respectively, for the selected days in January and August. The  
 286 corresponding SIC distributions for our retrievals are shown in Figure 11. On Figures 9 and 10, the  
 287 SIC values lower than 5% have been systematically omitted, for all estimates, including for the OSI  
 288 SAF results. No other filtering has been applied to our estimates (no coastal or atmospheric filtering).

289 Figures 9 and 10 show that the SIC spatial structures are globally very similar for all algorithms,  
 290 with the 6+10GHz results having the coarser spatial resolution, as expected. Our results do not show  
 291 obvious errors that would be related to the use of a unique set of tie points, regardless of the polar  
 292 regions and the season. Some unrealistic SICs are observed with the 18+36GHz algorithm, in regions  
 293 that are very likely ice-free (especially over the north polar region in August). If this algorithm was

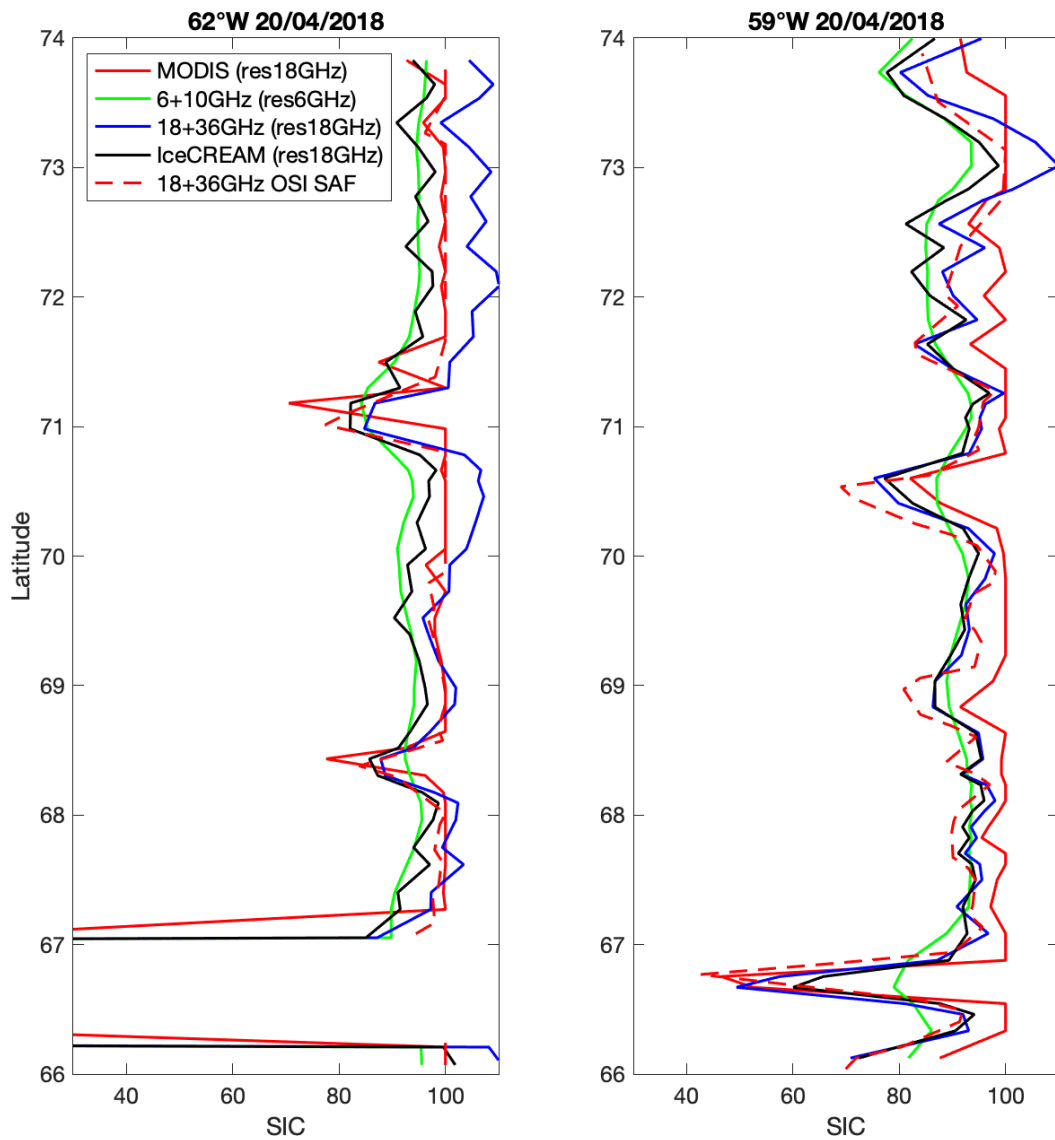


**Figure 8.** Transects over the scene, for different SIC estimates. Left: at 62°W. Right: at 59°W. The following products are compared: the MODIS estimates at 18 GHz resolution, our AMSR2 retrieval at 6+10GHz (at the spatial resolution of the 6 GHz) and at 18+36GHz (at the spatial resolution of the 18 GHz), the combination of these two results (the IceCREAM all channel results at the spatial resolution of the 18 GHz), and the OSI SAF operational products.

294 applied operationally, post filtering would be necessary. Combining all the frequencies with the  
295 IceCREAM scheme makes it possible to suppress the noisy signals of the 18+36GHz while benefiting  
296 from the high spatial resolution at these frequencies.

297 On August 30, the cloud cover was particularly dense over the Arctic high latitudes, especially  
298 south west of Greenland, likely associated with precipitation in some locations. This was confirmed  
299 with the help of the NASA viewing tool, <https://worldview.earthdata.nasa.gov>. The OSI SAF product  
300 erroneously detects a sea ice zone in the region of very thick clouds on that day (Figure 9, top right  
301 panel). We checked that the day before and the day after this structure was not present on the OSI  
302 SAF products. The algorithm based on the 18 and 36 GHz vertical polarizations is contaminated by  
303 the presence of clouds. Our 18+36GHz algorithm that uses both polarizations for the two frequencies  
304 is not seriously affected, and once combined with the 6+10GHz, it is clearly more robust to cloud  
305 contamination.

306 For the same two days and for both polar regions, the SIC distributions for the three retrievals  
307 (6+10GHz, 18+36GHz, and IceCREAM) are presented in Figure 11. Over these large regions, we  
308 expect a maximum of the SIC distribution at 0% and at 100%, and the departures of peak values in the  
309 distributions can be considered as biases. These biases have been systematically calculated for the four  
310 situations and for the three algorithms, along with the corresponding standard deviations (std) around  
311 these biases, and are added on Figure 11. For all the algorithms, the performances are better at 0%  
312 (lower bias and std) than at 100% SIC. In addition, the performances tend to be lower during summer  
313 than during winter in the considered region, especially for the 100% SIC. This is directly related to the  
314 melting conditions in summer, where the microwave signatures over ice can show larger variabilities  
315 than during winter. The 6+10GHz retrieval has almost always the best performances, at 0% and at  
316 100% SIC, both in terms of bias and standard deviation. On the contrary, the 18+36GHz algorithm  
317 has often the worse performances. Of course, in terms of spatial resolution, the 18+36GHz retrieval  
318 clearly defeats the 6+10GHz algorithm. With the same spatial resolution as the 18+36GHz algorithm,  
319 the performances obtained with IceCREAM are improved with respect to the 18+36GHz ones, and  
320 close to the 6+10GHz ones. IceCREAM successfully combines the low errors of the low frequency  
321 algorithm, with the high spatial resolution of the high frequency retrieval.

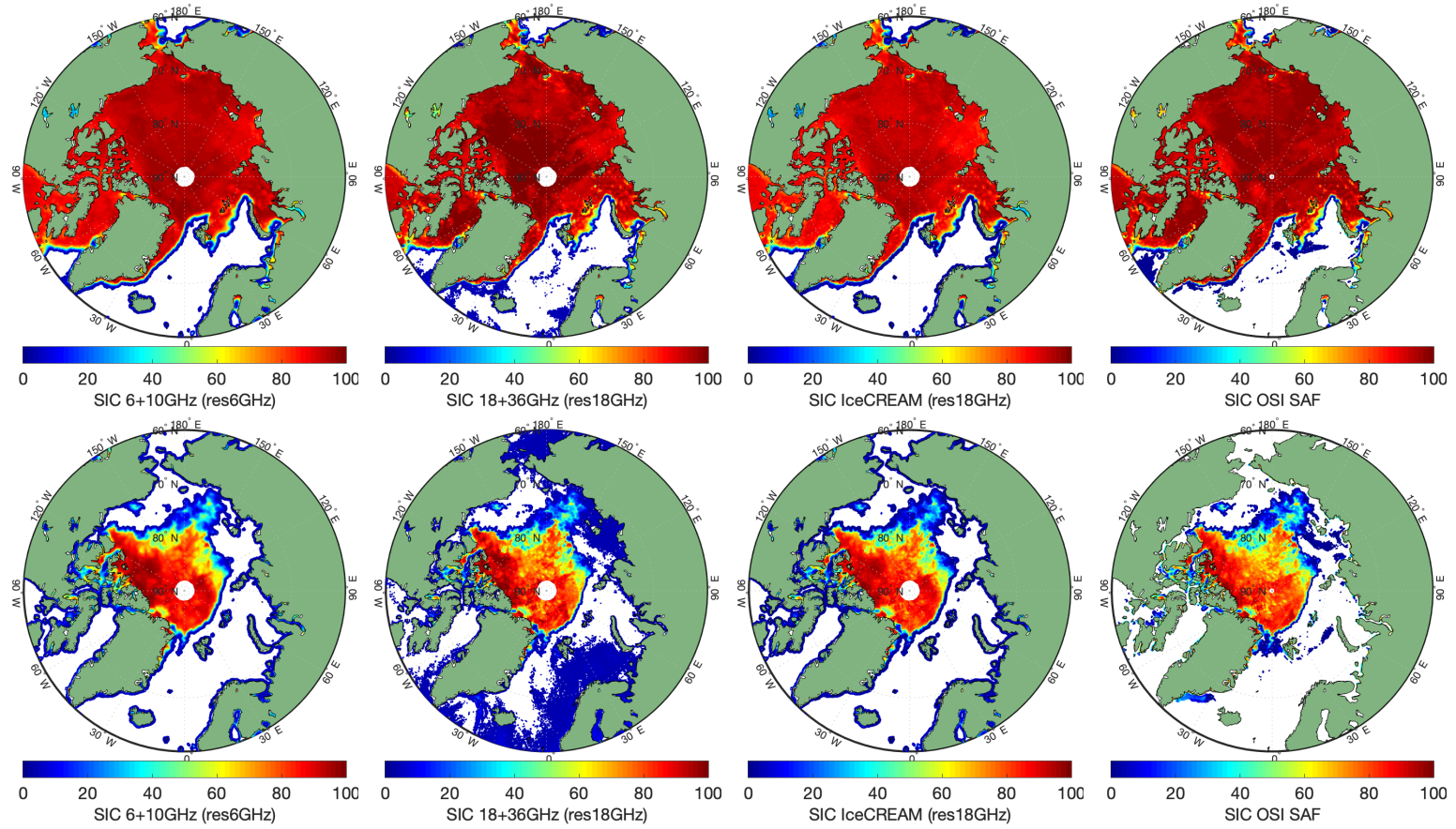


**Figure 9.** Over the north polar region, from left to right, comparison of our 6+10GHz and 18+36GHz algorithms, the all channel IceCREAM results, and the original OSI SAF estimates (using 18 and 36 GHz V polarization). Top: January 30, 2028. Bottom: August 30, 2018. Note that the values of SIC below 5% have been suppressed for all the estimates.



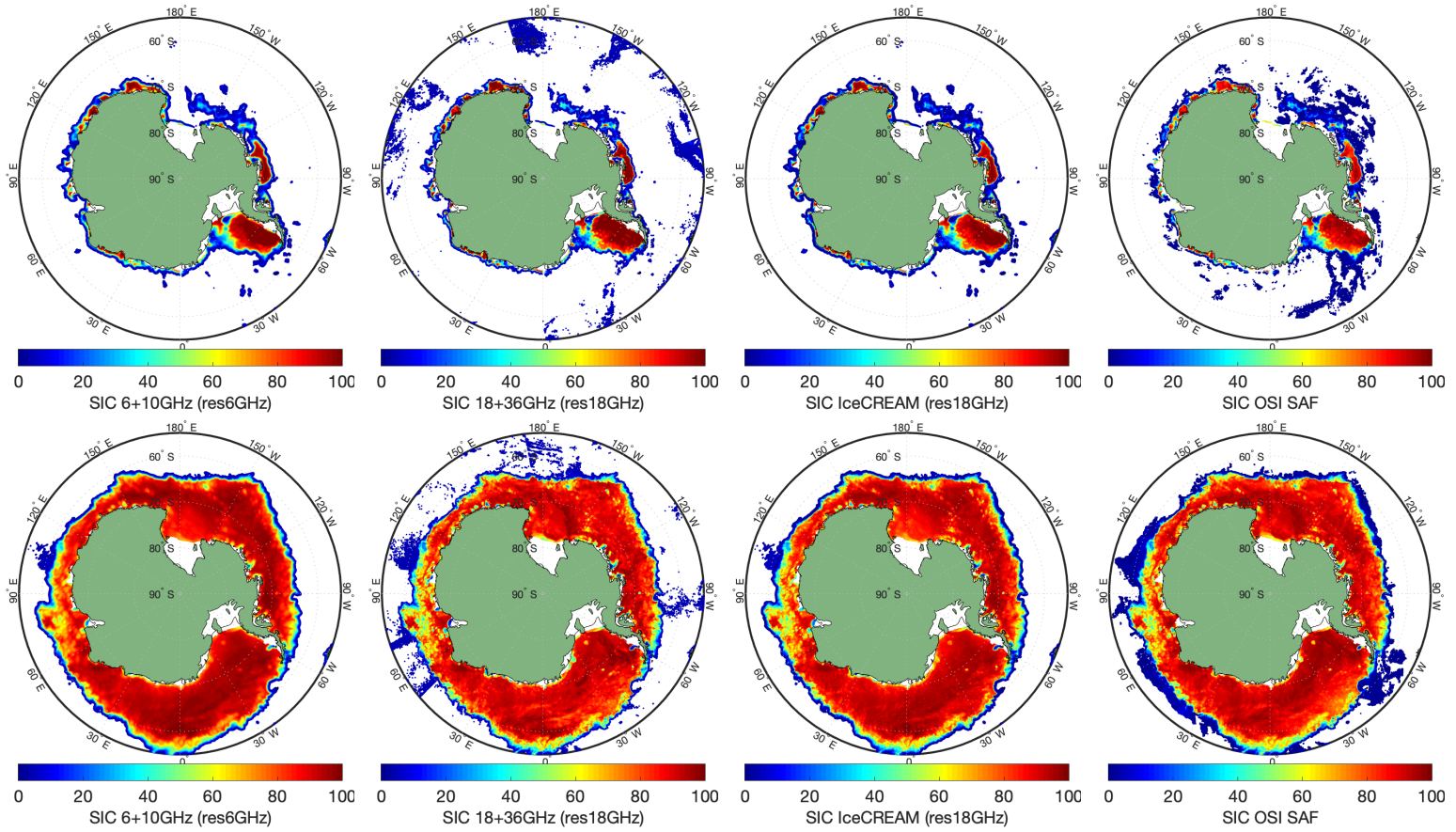


Figure 10. Same as Figure 9, over the south polar region.



## 5. Conclusions

A simple and flexible retrieval framework has been developed to estimate the SIC from passive microwave satellite observations between 6 and 36 GHz. It is based on the use of a collection of satellite observations at 0 and 100% SIC (the RRDP).

Different frequency combinations can be used, to minimize the uncertainty or to maximize the spatial resolution of the products. A solution is proposed here to optimize both, using all the frequency range from 6 to 36 GHz. It is a two step algorithm. First, the SIC is estimated at the low spatial resolution of the 6 GHz, using 6 and 10 GHz observations (both polarizations), and at the high spatial resolution of the 18 GHz, using the 18 and the 36 GHz (both polarizations). Second, the high spatial resolution 18+36GHz results within a low resolution 6+10GHz pixel are bias-corrected to match the 6+10GHz result, taking into account the respective errors of the products. This is the IceCREAM algorithm.

The algorithm is tested with AMSR2 observations, for a clear sky local scene with collocated MODIS estimates. It is also tested for the full polar regions, winter and summer, under clear and cloudy conditions. The OSI SAF operational product is also compared with our methodology. Our SIC results are very encouraging, providing both low errors related to the low frequency observations and high spatial resolution obtained from the high frequencies.

The method is developed for the CIMR project. It is evaluated here with AMSR2 observations. Better performances are expected with CIMR. First the spatial resolution of the instrument will be largely improved for all channels. Second, the 6 and 10 GHz (resp. the 18 and 36 GHz) will have the same resolution at  $\sim 15$  km (resp. at  $\sim 5$  km), making it natural to first exploit the collocated 6 and 10 GHz (resp. 18 and 18 GHz) observations before combining them.

Further refinements are expected in the near future, with the use of a radiative transfer model for the open ocean, to replace the RRDP information for the 0% situations. Development of an updated open ocean microwave emissivity model is underway. It builds upon recent work [21] showing that the current sea surface emissivity models still have difficulties under high wind speed conditions and in cold regions. It will reduce the uncertainty in the open ocean signature and it will duly account for the atmospheric contribution, using information from coincident Numerical Weather Prediction analysis. Once these improvements are implemented, the IceCREAM algorithm will be applied to the AMSR-E and AMSR2 collections over both polar regions.

**Author Contributions:** This study was conducted by C.P. and L.K., F.A. and V.P. have contributed to the development of the methodology, and C.J. has contributed to the discussions and to the writing of the paper.

**Funding:** This study has been partly supported by an ESA CIMR-APE contract, and by a TOSCA CNES support 'MICROWAT'.

**Acknowledgments:** JAXA AMSR2 L1R products are available from the file transfer protocol of the JAXA (<https://gportal.jaxa.jp/gpr/information/download>). The MODIS MYD29P1D data are extracted from the NASA site (<https://modis.gsfc.nasa.gov/data/dataproduct/mod29.php>). The OSI SAF AMSR2 product (OSI-408) has been downloaded from the OSI SAF site, hosted by Met Norway (<http://osisaf.met.no/p/ice/>). We thank Georg Heygster for very valuable discussions during this study. We also thank Craig Donlon and the Mission Advisory Group of the CIMR mission. We are grateful to three anonymous reviewers for their careful reading of the manuscript and interesting suggestions.

**Conflicts of Interest:** The authors declare no conflict of interest.

## References

1. Kilic, L.; Prigent, C.; Aires, F.; Heygster, G.; Pellet, V.; Jimenez, C. Ice Concentration Retrieval from the Analysis of Microwaves: A New Methodology Designed for the Copernicus Imaging Microwave Radiometer. *Remote Sensing* **2020**, *12*, 1060.
2. Simmonds, I. Comparing and contrasting the behaviour of Arctic and Antarctic sea ice over the 35 year period 1979-2013. *Annals of Glaciology* **2015**, *56*, 18–28.
3. Notz, D.; Stroeve, J. Observed Arctic sea-ice loss directly follows anthropogenic CO<sub>2</sub> emission. *Science* **2016**, *354*, 747–750.

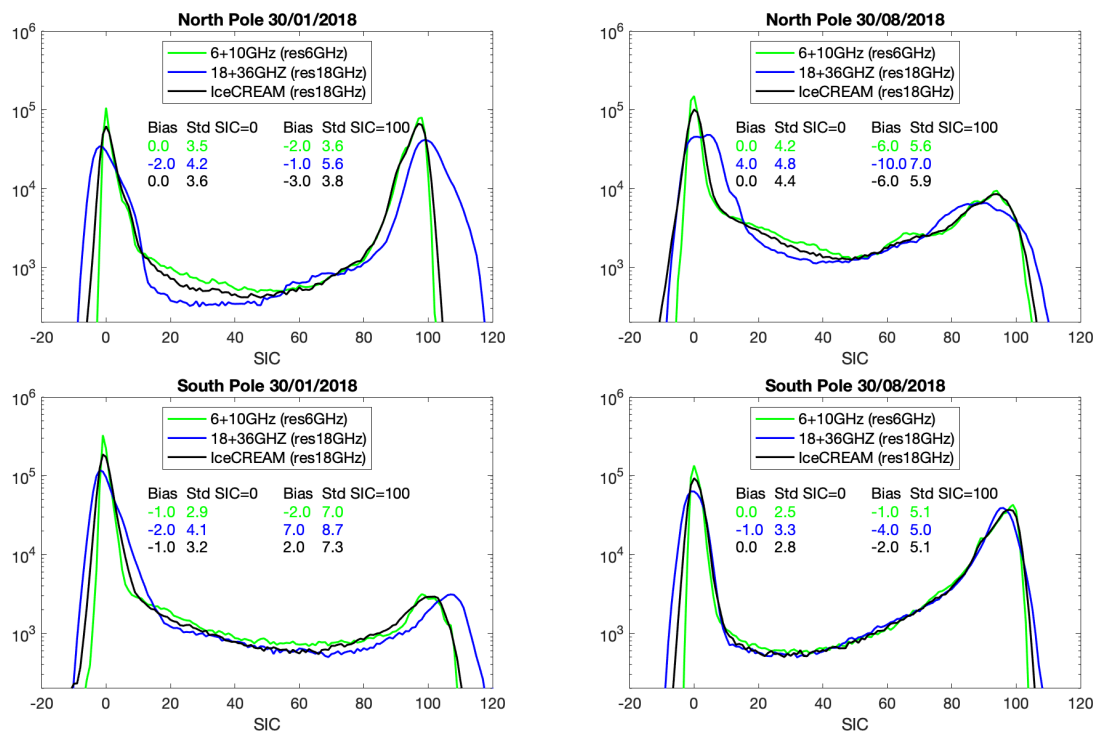


**Figure 11.** Histograms of our SIC estimates, for the north (top) and the south (bottom) polar regions, for January, 30, 2018 (left), and for August, 30, 2018 (right), for the 6+10GHz, the 18+36GHz, and the IceCREAM algorithms. A logarithmic scale is used for the y-axis. For SIC at 0% and SIC at 100%, the bias and the std are indicated for each algorithm, with the same color code. See the text for more detail.

- 372 4. Screen, J.A.; Simmonds, I. The central role of diminishing sea ice in recent Arctic temperature amplification. *Nature* **2010**, *464*, 1334–1337.
- 373
- 374 5. Dai, A.; Luo, D.; Song, M.; Liu, J. Arctic amplification is caused by sea-ice loss under increasing CO<sub>2</sub>. *Nature communications* **2019**, *10*, 1–13.
- 375
- 376 6. Screen, J.A.; Simmonds, I. Exploring links between Arctic amplification and mid-latitude weather. *Geophysical Research Letters* **2013**, *40*, 959–964.
- 377
- 378 7. Mori, M.; Watanabe, M.; Shiogama, H.; Inoue, J.; Kimoto, M. Robust Arctic sea-ice influence on the frequent Eurasian cold winters in past decades. *Nature Geoscience* **2014**, *7*, 869.
- 379
- 380 8. Luo, B.; Wu, L.; Luo, D.; Dai, A.; Simmonds, I. The winter midlatitude-Arctic interaction: effects of North Atlantic SST and high-latitude blocking on Arctic sea ice and Eurasian cooling. *Climate dynamics* **2019**, *52*, 2981–3004.
- 381
- 382
- 383 9. Tonboe, R.T.; Eastwood, S.; Lavergne, T.; Sørensen, A.M.; Rathmann, N.; Dybkjær, G.; Pedersen, L.T.; Høyer, J.L.; Kern, S. The EUMETSAT sea ice concentration climate data record. *The Cryosphere* **2016**, *10*, 2275–2290.
- 384
- 385 10. Pedersen, L.T.; Saldo, R. Sea Ice Concentration (SIC) Round Robin Data Package. Technical report, Sea Ice Climate Change Initiative, ESA, 2017.
- 386
- 387 11. Cavalieri, D.J.; Gloersen, P.; Campbell, W.J. Determination of sea ice parameters with the Nimbus 7 SMMR. *Journal of Geophysical Research: Atmospheres* **1984**, *89*, 5355–5369.
- 388
- 389 12. Comiso, J.; Sullivan, C. Satellite microwave and in situ observations of the Weddell Sea ice cover and its marginal ice zone. *Journal of geophysical research: Oceans* **1986**, *91*, 9663–9681.
- 390
- 391 13. Smith, D. Extraction of winter total sea-ice concentration in the Greenland and Barents Seas from SSM/I data. *Remote Sensing* **1996**, *17*, 2625–2646.
- 392
- 393 14. Lavergne, T.; Sørensen, A.M.; Kern, S.; Tonboe, R.; Notz, D.; Aaboe, S.; Bell, L.; Dybkjær, G.; Eastwood, S.; Gabarro, C.; others. Version 2 of the EUMETSAT OSI SAF and ESA CCI sea-ice concentration climate data records. *The Cryosphere* **2019**, *13*, 49–78.
- 394
- 395

- 396 15. Ivanova, N.; Pedersen, L.T.; Tonboe, R.T.; Kern, S.; Heygster, G.; Lavergne, T.; Sørensen, A.; Saldo, R.;  
397 Dybkjær, G.; Brucker, L.; Shokr, M. Inter-comparison and evaluation of sea ice algorithms: towards further  
398 identification of challenges and optimal approach using passive microwave observations. *The Cryosphere*  
399 **2015**, *9*, 1797–1817. doi:10.5194/tc-9-1797-2015.
- 400 16. Kilic, L.; Prigent, C.; Aires, F.; Boutin, J.; Heygster, G.; Tonboe, R.T.; Roquet, H.; Jimenez, C.; Donlon, C.  
401 Expected Performances of the Copernicus Imaging Microwave Radiometer (CIMR) for an All-Weather  
402 and High Spatial Resolution Estimation of Ocean and Sea Ice Parameters. *Journal of Geophysical Research:*  
403 *Oceans* **2018**, *123*, 7564–7580.
- 404 17. Rodgers, C.D. *Inverse methods for atmospheric sounding: theory and practice*; Vol. 2, World scientific, 2000.
- 405 18. Hall, D.K.; Riggs, G.A. MODIS/Aqua Sea Ice Extent 5-Min L2 Swath 1km. Version 6. *NASA National Snow*  
406 *and Ice Data Center Distributed Active Archive Center, Boulder, Colorado USA* **2015**, *10*.
- 407 19. Maeda, T.; Taniguchi, Y.; Imaoka, K. GCOM-W1 AMSR2 level 1R product: Dataset of brightness  
408 temperature modified using the antenna pattern matching technique. *IEEE Transactions on Geoscience and*  
409 *Remote Sensing* **2016**, *54*, 770–782.
- 410 20. Comiso, J.; Cavalieri, D.J.; Parkinson, C.L.; Gloersen, P. Passive microwave algorithms for sea ice  
411 concentration: A comparison of two techniques. *Remote sensing of Environment* **1997**, *60*, 357–384.
- 412 21. Kilic, L.; Prigent, C.; Boutin, J.; Meissner, T.; English, S.; Yueh, S. Comparisons of Ocean Radiative Transfer  
413 Models With SMAP and AMSR2 Observations. *Journal of Geophysical Research: Oceans* **2019**, *124*, 7683–7699.  
414 doi:10.1029/2019JC015493.

415 © 2020 by the authors. Submitted to *Remote Sens.* for possible open access publication  
416 under the terms and conditions of the Creative Commons Attribution (CC BY) license  
417 (<http://creativecommons.org/licenses/by/4.0/>).